Planetary boundary layer height modulates aerosol – water interactions during winter in the megacity of Delhi

Subha S. Raj[1,2], Ovid O. Krüger[3], Amit Sharma[1,a], Upasana Panda[1,4], Christopher Pöhlker[3], David Walter[3], Jan-David Förster[3], Rishi Pal Singh[5], Swetha S.[1,b], Thomas Klimach[3], Eoghan Darbyshire[6,c], Scot T. Martin[7,8], Gordon McFiggans[6], Hugh Coe[6], James Allan[6,9], Ravikrishna R.[10,2], Vijay Kumar Soni[5], Hang Su[3], Meinrat O. Andreae[3,11,12], Ulrich Pöschl[3], Mira L. Pöhlker[3]and Sachin S. Gunthe[1,2]

[1]EWRE Division, Department of Civil Engineering, Indian Institute of Technology Madras, Chennai, India
[2]Laboratory for Atmospheric and Climate Sciences, Indian Institute of Technology Madras, Chennai, India
[3]Multiphase Chemistry and Biogeochemistry Department, Max Planck Institute for Chemistry, Mainz, Germany
[4]Department of Environment and Sustainability, CSIR Institute of Minerals and Materials Technology, Bhubaneswar, India
[5]India Meteorological Department, New Delhi, India
[6]Department of Earth and Environmental Sciences, School of Natural Sciences, University of Manchester, Manchester, UK
[7]John A. Paulson School of Engineering and Applied Sciences, Harvard University, Cambridge, MA, USA
[8]Department of Earth and Planetary Sciences, Harvard University, Cambridge, MA, USA
[9]National Centre for Atmospheric Science, University of Manchester, Manchester, UK
[10]Department of Chemical Engineering, Indian Institute of Technology Madras, Chennai, India
[11]Scripps Institution of Oceanography, University of California San Diego, La Jolla, CA, USA
[12]Department of Geology and Geophysics, King Saud University, Riyadh, Saudi Arabia
[a]now at: Department of Civil and Infrastructure Engineering, Indian Institute of Technology Jodhpur, Karwar, Jodhpur, India
[b]now at: CSIR Fourth Paradigm Institute, Bengaluru, India
[c]now at: The Conflict and Environment Observatory, Hebden Bridge, West Yorkshire, UK

Key Points:

- Parameterizing the relation between planetary boundary layer height and CCN loading.
- Parameterization of CCN activity.
- Major driving force of aerosol accumulation and aging processes in Delhi during winter is planetary boundary layer height.

Corresponding author: Subha S. Raj, `subhasraj89@gmail.com`

Corresponding author: Mira L. Pöhlker, `m.pohlker@mpic.de`

Corresponding author: Sachin S. Gunthe, `s.gunthe@iitm.ac.in`

Abstract

The Indo-Gangetic Plain is one of the largest sources of air pollution worldwide, and throughout winter strong fluctuations in the planetary boundary layer (PBL) height, driven by a strong radiative thermal inversion, affect the dispersion of this pollution. To date, tie-ins into aerosol-water vapour interactions, especially cloud condensation nuclei (CCN) activity, and the associated implications for aerosol indirect effects and hence on regional and global climate have been little studied. We present the results of a one-month field campaign (February-March 2018) in the polluted megacity of Delhi. The composition of fine particulate matter (PM1) and size-resolved CCN properties were measured over a wide range of water vapour supersaturations. PBL modelling, backward trajectories, and fire spots were included in the analysis to elucidate the influence of PBL and air mass origins on the aerosols. The aerosol properties depended strongly on the PBL height, with enhanced PM1 concentrations, high mass fractions of organic matter and BC, and low aerosol hygroscopicity during time periods of low PBL height (<100 m). The observed correlations of PM1, aerosol particle number and CCN number with PBL height were parameterized by simple power law fit. Changes in PBL height induced changes in aerosol accumulation and aging processes, as manifested in aerosol composition and hygroscopicity. In contrast, aerosol properties did not depend strongly on air mass origins or wind direction, implying that the observed aerosol and CCN represented local emissions. The relationship between CCN number and supersaturation was well described by an error function parameterization.

1 Introduction

The megacity of Delhi is located within the Indo-Gangetic Plain (IGP) and is one of the major sources of anthropogenic air pollution. It is a landlocked metropolitan area in a large valley south of the Himalayas, which causes the air masses to be constrained within the IGP during most of the year (Figure 1). The air masses are vulnerable to high levels of particulate matter emissions from the megacity all year round (Bhandari et al., 2020), since it is a fast-growing urban agglomeration (Jain et al., 2016; Paul et al., 2021). During the winter season, the shallow planetary boundary layer (PBL) due to radiative thermal inversion in the nighttime and the resulting high relative humidity (RH), coupled with low wind speeds and high aerosol mass burden, makes the landlocked atmosphere conducive to fog formation (Arun et al., 2018; Ojha et al., 2020; Thomas et al., 2019; Tiwari et al., 2013). The companion study of Gunthe et al. (2021) reported that the aerosols in Delhi have enhanced water uptake ability, which can further facilitate multiphase formation of aerosols. Aerosol – PBL interactions can lead to fog and haze formation during winter (Cheng et al., 2016; H. Su et al., 2020; T. Su et al., 2020; Tie et al., 2017; Zheng et al., 2015). Such megacities have enhanced concentration of fine aerosol particulate matter, which are detrimental to public health (Lelieveld et al., 2020), and extensive anthropogenic gaseous emissions further affect aerosol cloud activation responses.

The spatial heterogeneity of cloud condensation nuclei (CCN) activity is not suitably captured in the sub-grids of climate models, which causes uncertainties in the estimates of their atmospheric responses to climate change (Boucher et al., 2013). This uncertainty is expected to be large in the Indian sub-continent due to the variety of topographical features like high mountains, low lying coastal plains, the peninsular plateau; and human settlements ranging from rural towns and villages to metropolitan cities. In addition, over the megacity of Delhi, meteorological processes and features are very much different than those of other megacities around the world. For example, the radiative cooling of the surface during winter causes aerosol accumulation within a shallow surface layer (Dumka et al., 2019; Ojha et al., 2020; Raatikainen et al., 2011; Tiwari et al., 2013) and induces fog formation over Delhi, in contrast with frontal inversion and alternative temperature advective processes over other megacities across the globe (T. Su et al., 2020; Yu et al., 2020; Zheng et al., 2015). Nevertheless, realistic formulations of CCN activity are not yet reported over this region for effective prediction to be used in prognostic climate models. Observations of

CCN activity is a proxy for aerosol - water vapour interaction, which may further strongly influence and govern the fog and haze formation ability of aerosols and multiphase processes.

To capture the nuanced interaction of aerosols with atmospheric water vapour, which leads to cloud, fog and haze formation, and health impacts, field measurements are essential. At present we have a fair understanding of CCN activity from size-resolved CCN measurements under diverse environmental conditions, from clean Amazonian rainforest (Gunthe et al., 2009; Pöhlker et al., 2016, 2018) to highly polluted megacities like Beijing (Gunthe et al., 2011) and Guangzhou (Rose et al., 2010, 2011) in China and other locations (Asa-Awuku et al., 2015; Atwood et al., 2017; Bhattu et al., 2016; Che et al., 2017; Henning et al., 2014; Iwamoto et al., 2016; Ma et al., 2017). Here we present a comprehensive study of aerosols using size-resolved CCN measurements, supplemented by concomitant non-refractory PM1 (NR-PM1) composition and black carbon (BC) observations conducted within the metropolitan area of Delhi. From the 27-day long campaign in Feb to Mar 2018, we investigated and identified the meteorological factors playing a major role in transforming aerosol chemistry and retrieved CCN activity parameterizations validated against field measurements. During this short period, we witnessed two contrasting meteorological events characterized by the extent of temperature inversion, which are further termed as strong and weak radiative inversion periods for the ease of reading. The resulting strong contrast in PBL height in such a short duration revealed some interesting insights of the aerosol interaction with water vapour and the subsequent cloud activation response in the confined atmosphere of Delhi under varied aerosol emissions.

There have been no direct measurements of CCN properties in size resolved mode over this part of the globe. However, there are a few studies investigating CCN properties based on e.g. aerosol mass spectrometer and visibility data (Arub et al., 2020; Wang & Chen, 2019). The previous attempts on measurement of CCN properties were largely limited to regions close to Delhi (Bhattu et al., 2016; Jayachandran et al., 2020). This study reports direct measurements of aerosol hygroscopicity and CCN activity derived from size resolved CCN measurements in Delhi. Previous studies on atmospheric aerosols in general, but not on CCN, in Delhi have reported that primary sources of NR-PM1 such as biomass burning (BB) and fossil fuel combustion (Arub et al., 2020) are dominant, along with a major PM contribution from secondary aerosol formation all year round (Gani et al., 2019; Jaiprakash et al., 2017). Episodic peaks in primary organic aerosols along with ammonium chloride were reported previously by Gani et al. (2019) and Bhandari et al. (2020), as well as the companion study by Gunthe et al. (2021). Studies on the influence of meteorology on aerosol properties show that in spite of sources remaining unchanged, the extreme lowering of the PBL below 100 m during winters brings particulate matter concentrations to hazardous levels (Bhandari et al., 2020; Dumka et al., 2019; Gani et al., 2019; Mandal et al., 2014; Murthy et al., 2020; Ojha et al., 2020). The influence of air mass history has also been reported using back trajectory analysis (Arub et al., 2020; Jaiprakash et al., 2017). A comprehensive analysis provided in this study combining air mass back trajectory analysis as well as identification of wildfire and BB locations (see Sect. 2.2) and meteorology with CCN activity of aerosols is unprecedented.

2 Methods and supplementary analysis

2.1 Measurement site, local meteorology and experimental setup

Simultaneous measurements of size-resolved CCN, chemical composition of non-refractory PM1 (NR-PM1), and black carbon mass concentration (AE33) were conducted as part of the Atmospheric Pollution and Human Health Program under Process Analysis, Observations and modelling – Integrated Solutions for Cleaner Air for Delhi (APHH – PROMOTE) campaign. The field campaign was conducted towards the end of winter in 2018 from 05 Feb to 02 Mar and the measurement site was situated inside the campus of the India Meteorological Department, Delhi (28.5886°N, 77.2219°E; 214 m a.s.l., Fig. 1), located amidst the metropolitan area. Delhi is enclosed by the Thar desert (Rajasthan) to the

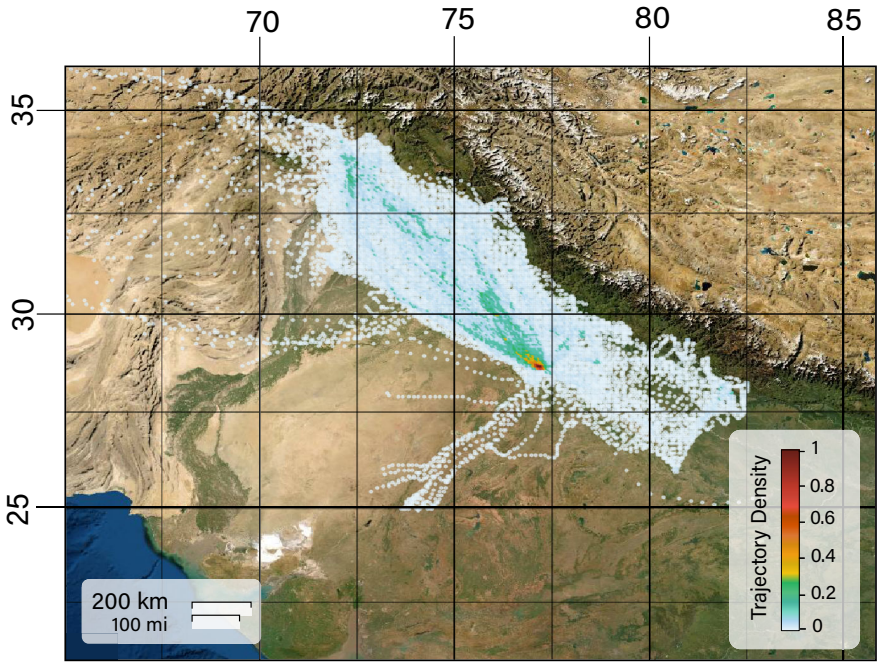

Figure 1. The air mass backward trajectories up to 3 days during the campaign period (Feb-Mar 2018), colour-scaled by the trajectory density in the occupied grid (0.1°x 0.1°grid). A trajectory density of 1 indicates all sampled air masses passed through the indicated location. The map layer used is retrieved from ESRI (https:// services.arcgisonline.com/ ArcGIS/ rest/ services/ World Imagery/ MapServer/ tile/ z/ y/ x).

west, the Deccan plateau to the south, and is located in front of the Himalayan mountain range, which extends from the north of Delhi to the far north east. The metropolitan area of Delhi is an extensively built-up area accommodating numerous small and large industries and transportation facilities, including a busy international airport which is at a distance of ∼10 km (Guttikunda & Calori, 2013; Jain et al., 2016) from the campaign location.

The climate in Delhi is semi-arid with very hot summers, moderate monsoon, and cold winters. The winter is from early November to mid-February characterized by moderately cold days, and cold and humid nights resulting in a distinct radiative thermal inversion (Arun et al., 2018; Dumka et al., 2019; Kumar et al., 2017; Ojha et al., 2020; Raatikainen et al., 2011; Thomas et al., 2019). In the present study we used the meteorological data collected at the Indira Gandhi International Airport (https://www.ncdc.noaa.gov/). The average diurnal temperature (T) cycled between 10 and 25 °C and the average diurnal RH from 26 to 90 %. The meteorological data at the airport showed a strong correlation (R^2 >0.97) with the quasi-continuous data measured at the observation site. Therefore, as the data from the airport is continuously available, we used these in the present study for all the analyses requiring meteorological data.

The aerosol measurement instruments were placed in an air-conditioned container, fitted with a stainless-steel inlet ∼5 m above the ground. The inlet tubing was smoothly bent so that the cover of the meshed opening was upside down to bar the entry of rainwater and other debris. The aerosol samples were dried so that the moisture content was below ∼25 % RH using a diffusion drier containing silica gel (Merck, Germany; ∼1 - 3 mm size). Thereafter the polydisperse aerosol flow was divided using a 'Y'-shaped splitter and used to supply (i) an aerosol number size distribution, and size-resolved CCN setup; and (ii)

a chemical composition measurement setup. The temperature inside the container was maintained at ∼28 °C throughout the campaign to ensure a stable working environment for the instruments.

2.2 Back trajectory and fire spot analysis

The spatiotemporal pattern of air masses over Delhi was studied using 3-day back trajectory (BT) data, retrieved using the HYSPLIT (The Hybrid Single-Particle Lagrangian Integrated Trajectory) model (Stein et al., 2015). Three years of data (1 Jan 2016 to 31 Dec 2018), which constituted 26304 number of BTs, with each BT containing 73 latitude-longitude data pairs were clustered spatially using the Quickbundles algorithm (Garyfallidis et al., 2012) in Python (Van Rossum & Drake, 2009). It is a fast clustering method, for simplifying complex and large sets of tractography data. Quickbundles has a built-in metric called the minimum average direct-flip distance (MDF), which selects the minimum among the Euclidean distance between trajectories determined using two methods, one that considers points that lie in the same sequential position and another that considers points lying in opposite sequence in both trajectories. MDF efficiently separates the BTs based on length as well as direction. Based on this algorithm and subsequent analysis results, we identified nine major BT cluster directions in a year. Out of this, only three could be mapped for the time of the year we conducted the measurements. They were north-west (NW), south-east (SE) and mixed regional pollution (MRP).

The most frequently sampled air mass during the campaign belonged to NW, which gave us 540 samples in the size-resolved CCN experiment (or CCN scans), followed by MRP which gave 149 scans, and SE which gave 44 scans, out of the total 733 good-quality CCN scans. The density of BTs in a grid of 0.1°x 0.1°was also calculated and plotted (Fig.1) using a program written in Python. To complement the above BT analysis, fire intensity ($\mathrm{W\,m^{-2}}$) maps were retrieved from Copernicus Atmosphere Monitoring Service (CAMS) - Global Fire Assimilation System (GFAS). The data was in NetCDF3 format and the graphs were visualized in QGIS overlaid on a geo-referenced map layer of India. During the measurement period, the fire spot data analysis revealed a series of small fire events much farther than the consistent fire spots present over Punjab and Haryana, which generally affect air quality in Delhi during the stubble burning period of Oct-Nov. Our fire spot analysis further confirms the presence of fire spots in Oct and Nov-2017 preceding our campaign.

2.3 Planetary boundary layer modelling

The Weather Research and Forecasting model (WRF version 4.0) was used to simulate diurnal variation in planetary boundary layer height (H_{BL}). The centre of the model domain is at 76°E, 29°N and there are 240 grid points in the east-west direction and 147 grid points in the north-south direction on a Mercator projection, along with 51 vertical levels. Model simulations are conducted at a resolution of 12 km x 12 km. Initial and lateral boundary conditions for the meteorological fields were prepared using the Era Interim data (https:// www.ecmwf.int/ en/ forecasts/ datasets/ reanalysis-datasets/ era-interim). Model simulation was conducted for the period of 1 Feb 2018 to 3 Mar 2018 at a time step of 72 s and the model output was stored every hour for analysis. The first 4 days of model output have been discarded to account for model spin-up. Physics schemes used in the model to parametrize different processes were: i) Lin et al. scheme for cloud microphysics; ii) Grell 3D ensemble scheme for cumulus parameterization; iii) Unified Noah land surface model for land surface option; iv) Rapid radiative transfer model for long wave radiation; v) Goddard shortwave scheme for short wave radiation and vi) Mellor-Yamada-Janjic scheme for planetary boundary layer. The model results (Raj et al., 2021) were found to be in strong agreement with the ceilometer quasi-continuous measurements carried out at the same location as part of this campaign.

3 Instrumentation and data analysis

3.1 Size-resolved CCN measurements

The size-resolved CCN experiment was carried out based on Frank et al. (2006) and Rose et al. (2008), by the coordinated controlling of three instruments viz., a Cloud Condensation Nuclei Counter (CCNC, model CCN-100, DMT; Roberts and Nenes (2005)) to estimate total CCN number concentration, an electrostatic classifier (EC, model 3080, TSI) with a differential mobility analyzer (long DMA, model 3081, TSI) to select monodisperse aerosol particles, and a condensation particle counter (UCPC, model 3776, TSI) to count total aerosol particles. The entire setup was controlled externally by a computer which runs a dedicated, in-house developed, and well tested LabVIEW (National Instruments, Munich, Germany) program (Pöhlker et al., 2016) to continuously sample ambient aerosols of the size range relevant to cloud processing (26 size bins or mobility diameters (D) in the range, 10 to 370 nm) and measure cloud activation at different supersaturation (S) levels.

The dried polydisperse aerosol samples were drawn into the EC, where they are passed through a radioactive neutralizer (Kr-85, model 3077A, TSI) to attain a known charge distribution. The charged particles were then passed through an electric field inside the long-DMA, where they were segregated based on their electrical mobility. The DMA was controlled by the LabVIEW program to set the appropriate voltage in order to select the desired D and produce a near-monodisperse aerosol flow. This flow was further split, using a 'Y'- shaped connector tube, between CCNC and UCPC to measure CCN and total aerosol number concentration for a chosen diameter. The DMA maintained the near-monodisperse flow of selected D for 30 s, then switched to the next D after flushing off the DMA's column for 40 s to make it particle-free. Meanwhile, the CCNC was controlled to maintain a specific S level for a duration of 40 min, to let all D to pass through the instruments. While the CCNC measured the particles in D activated as cloud droplets (greater than 1 μm) at the S level attained inside the CCNC column ($N_{\mathrm{CCN}}(S,D)$), the UCPC simultaneously measured the total particle number concentration for a given D ($N_{\mathrm{CN}}(D)$). A relevant set of 11 selected S levels were cycled in the CCNC column by providing an equilibration time of 5 min for each S, taking ∼8 hrs to finish a complete cycle of S levels.

The sample flow through the DMA was 0.8 L min^{-1}, which includes the 0.3 L min^{-1} to the UCPC and 0.5 L min^{-1} to the CCNC. The sheath to sample flow ratio inside the DMA was 7.5, and the total flow to aerosol flow ratio inside the CCNC was 10. The liquid supply pump was working in the low flow mode with a supply of 4 mL h^{-1}. The size-resolved CCN experiment setup measured aerosol samples at temperature 299 ± 2.3 K, pressure 959 ± 8.2 hPa, and $25\,\% \pm 5\,\%$ *RH* (arithmetic mean ± standard deviation).

The CCNC was systematically calibrated based on Rose et al. (2008) for different S levels before and after the 27-day campaign (02 Feb 2018 and 03 Mar 2018). Calibrations were performed using standard ammonium sulphate aerosols, whose cloud droplet activation is well explained using classic Köhler theory. Standard ammonium sulphate aerosols were generated by nebulizing an aqueous salt solution (0.3 g L^{-1}) of ammonium sulphate ($(NH_4)_2SO_4$, purity >99.5 %) in a TSI Aerosol Generator. Both calibration experiments gave a similar relationship between the S level estimated experimentally (or effective supersaturation, S_{eff}) and the corresponding measured temperature gradient (dT, K) inside the CCNC column. This ensured the stable functioning of the CCNC during the campaign period. All S levels at which parameters are reported in this paper refer to experimentally derived S_{eff}.

3.2 Measurement specifications

It should be noted that the measurements made in the study are not purely ambient, due to the conditioning of aerosol samples taken from the atmosphere to a moisture content below 25 % *RH*. It is strongly possible that there are losses of volatile species during the passage of the air through the chambers of the various instruments, which are operated at a fixed temperature. Nevertheless, the measurements reported should be considered

as the intrinsic properties of aerosols at the following atmospheric conditions, $T = 299 \pm 2.3\,\mathrm{K}$, $P = 959 \pm 8.2\,\mathrm{hPa}$ and $RH = 25\,\% \pm 5\,\%$ (arithmetic mean $\pm$ standard deviation measured during campaign). To convert to standard conditions (STP: 273 K, 1000 hPa, 0 % RH), the reported values can be multiplied by a factor of 1.08 (derived using the ideal gas law). However, this correction does not account for the change in particle size, mass and hygroscopicity due to loss of volatile species, interaction with gaseous phase components, and gas - particle partitioning.

3.3 Data analysis of size-resolved CCN measurements

Size-resolved CCN measurements provide the cloud activated fraction ($N_{\mathrm{CCN}}(S,D)/N_{\mathrm{CN}}$) for a selected D at the S level attained in the CCNC column. Each $N_{\mathrm{CCN}}(S,D)/N_{\mathrm{CN}}$ value plotted against the corresponding D for the measured S level gives a CCN activation curve, which constitutes a measured scan. The average CCN activation curves measured at each S level are shown in Figure 2. The most important parameter obtained from these curves is the midpoint activation diameter ($D_{\mathrm{a}}(S)$), which is the minimum diameter required for activation of 50 % of condensation particles in the sample at given S level. Over the course of the entire campaign, 744 scans were measured and analyzed to calculate CCN properties based on the theories put forth in Petters and Kreidenweis (2007) and Rose et al. (2008). Based on the quality of data, only 733 scans (Raj et al., 2021) were selected for further analyses and representation in this study.

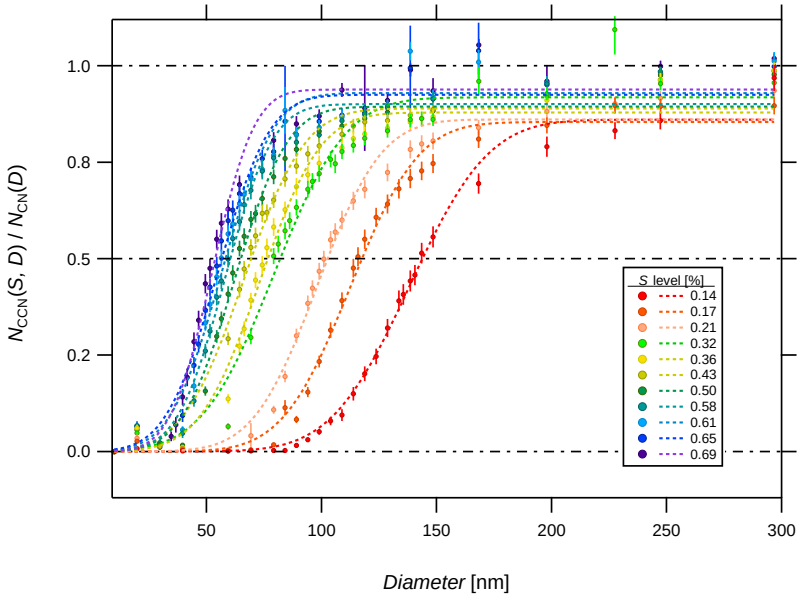

Figure 2. Campaign-average data points of CCN activation across selected size bins for all measured S levels. The dashed coloured lines are the single-erf fit based on Rose et al. (2008)

3.4 Errors and corrections in size-resolved CCN data

Practical limitations of the instruments generally introduce errors in the measured mobility diameter of particles and activated fractions. The outlet slit of the DMA is relatively larger than the particles and hence it permits a size bin, rather than a fixed size in the outflow (Knutson & Whitby, 1975). Moreover, some of these particles carry multiple charges and attain enhanced electrical mobility inside the DMA. These multiple-charged particles flow along with smaller single-charged particles of similar electrical mobility resulting

in enhanced activated ratios and induce errors. Thus measured activated fractions were carefully corrected for multiple-charged particles based on Frank et al. (2006), by taking into account the presence of up to quadruple-charged particles. Following Rose et al. (2008) these corrected fractions were used to back-calculate the measured diameter, by applying the transfer function, which is the probability of a certain D passing through the DMA's slit (Knutson & Whitby, 1975). The corrected activation curves were fitted with a 3-parameter cumulative distribution function (CDF) using the non-linear least squares fitting routine (Gauss-Newton method, Matlab, MathWorks, Inc.) defined by the parameters: $D_{\mathrm{a}}(S)$; $N_{\mathrm{CCN}}(S,D)/N_{\mathrm{CN}}$ at 50 % activation or $a(S,D)$; and the width of the activation curve or $\sigma(S)$ (Rose et al., 2008).

3.5 Size data inversion for particle number size distribution

Due to instrumental limitations the routinely measured aerosol particle number size distribution could not be used for further analysis. Therefore, alternatively we used the aerosol number size distribution obtained by the inversion of $N_{\mathrm{CN}}(D)$ data retrieved using size-resolved CCN measurements. A dedicated inversion routine was developed (Matlab, MathWorks, Inc.) following the method and approximations described by Wiedensohler (1988).

The measured $N_{\mathrm{CN}}(D)$ is the concentration of particles in a narrow size bin, D, governed by the electrical mobility of the particles inside the DMA. Since the DMA used had a negatively charged electrode, $N_{\mathrm{CN}}(D)$ was the concentration of only the positively charged particles. Moreover, the UCPC measures only half the original concentration of positively charged particles, owing to the triangular nature of the transfer function (Knutson & Whitby, 1975). Hence two times the value of $N_{\mathrm{CN}}(D)$ is used to account for this loss. The inertial impactor at the sampling inlet of DMA ensures that only those particles less than a given cut diameter enter the instruments, and the largest size bin (D_{max}) sampled was approximately equal to this cut diameter. Therefore, the concentration at D_{max}, $N_{\mathrm{CN}}(D_{\mathrm{max}})$ corresponds to only +1 charged particles, so it required no multiple charge correction.

In order to calculate near-ambient particle concentration, the measured $2^{*}N_{\mathrm{CN}}$ values are divided by the probability of the radioactive neutralizer generating particles of charge e = +1 in each D (Wiedensohler, 1988). This quantity, when calculated for all D except D_{max}, includes particles carrying multiple charges in the range, e = [-4, +4]. So the multiple charge correction is applied for up to 2 charges using Wiedensohler coefficients (Wiedensohler, 1988) and for 3 to 4 charges using Gunn's equation (Gunn, 1954).

The inverted size distribution was compared with quasi-continuous parallel measurements of aerosol number size distribution using an SMPS consisting of an electrostatic classifier (EC, model 3082, TSI) with Nano DMA (model 3085, TSI) and a condensation particle counter (CPC, model 3772, TSI). Although the measured size range of the Nano-SMPS was 8 to 105 nm, it served as a quality check for the inverted particle concentration in that size range. The qualitative match of the inverted size distribution was in good agreement, with about a 30 % reduction in number, which is expected due to the size-resolved mode of measurement, where the mobility diameter was selected step-wise unlike the continuous scanning mode done in SMPS. Hence in order to take this loss into account, the inverted particle number size distribution ($\mathrm{d}N/\mathrm{dlog}D$) and particle concentrations in the size range 10 to 370 nm ($N_{\mathrm{CN,10}}$) reported in this paper have been up-scaled by a factor of 1.3 (Raj et al., 2021).

3.6 CCN properties

The parameters of the CDF fit to the activation curves, along with S_{eff} and particle number size distribution were used to calculate key CCN properties (as enumerated below) based on literature. Average CCN properties measured during the field campaign are tabulated as a function of experimentally derived S levels in Table 1.

Table 1. CCN properties measured during Feb - Mar 2018 at Delhi shown as a function of effective supersaturation achieved inside the CCNC. The S levels are average values, and all had a standard deviation of ∼0.001. All other values are expressed as average ± standard deviation. Parameters tabulated are: midpoint activation diameter ($D_a(S)$), hygroscopicity from size-resolved CCN measurements ($\kappa(S, D_a)$), width of the CCN activation curve ($\sigma(S)$), maximum activated fraction ($MAF(S)$), total CCN concentration ($N_{CCN}(S)$), total particle concentration in the size range ∼10 to 370 nm ($N_{CN,10}$), CCN efficiency ($N_{CCN}(S)/N_{CN,10}$), and number of samples for each S levels (n).

S [%]	$D_a(S)$ [nm]	$\kappa(S, D_a)$	$\sigma(S)$ [nm]	$MAF(S)$	$N_{CCN}(S)$ [cm^{-3}]	$N_{CN,10}$ [cm^{-3}]	$N_{CCN}(S)$ /$N_{CN,10}$	n
0.14	141 ± 14	0.28 ± 0.09	26 ± 9	0.85 ± 0.16	4341 ± 2607	17789 ± 9460	0.26 ± 0.10	65
0.17	115 ± 10	0.31 ± 0.08	23 ± 8	0.86 ± 0.16	5959 ± 3268	16550 ± 8414	0.37 ± 0.12	70
0.21	101 ± 9	0.31 ± 0.08	25 ± 10	0.89 ± 0.14	7230 ± 3883	16772 ± 8708	0.45 ± 0.13	69
0.32	80 ± 7	0.27 ± 0.07	22 ± 8	0.90 ± 0.12	9143 ± 5136	16861 ± 9213	0.55 ± 0.12	67
0.36	75 ± 8	0.27 ± 0.09	20 ± 10	0.90 ± 0.13	10149 ± 5839	17592 ± 9571	0.59 ± 0.12	67
0.43	68 ± 7	0.25 ± 0.07	21 ± 7	0.91 ± 0.13	10800 ± 6148	17672 ± 9449	0.62 ± 0.14	64
0.50	64 ± 7	0.22 ± 0.07	18 ± 9	0.91 ± 0.12	11721 ± 6708	18117 ± 9371	0.65 ± 0.13	63
0.58	60 ± 8	0.21 ± 0.10	18 ± 8	0.92 ± 0.12	12277 ± 7497	18100 ± 9796	0.68 ± 0.13	65
0.61	58 ± 8	0.20 ± 0.08	19 ± 10	0.92 ± 0.12	12493 ± 6987	18492 ± 9268	0.68 ± 0.14	64
0.65	56 ± 8	0.20 ± 0.10	17 ± 8	0.92 ± 0.12	12959 ± 6620	18941 ± 9218	0.70 ± 0.13	62
0.69	54 ± 8	0.20 ± 0.11	15 ± 8	0.94 ± 0.10	13252 ± 7147	18486 ± 8920	0.72 ± 0.12	65

1. Effective hygroscopicity parameter of the aerosol population: $\kappa(S,D_a)$
   The measured $D_a(S)$ and corresponding S_{eff} were used in κ-Köhler theory (Petters & Kreidenweis, 2007) to calculate the effective hygroscopicity parameter $\kappa(S,D_a)$, which encompasses all the composition dependent variables (Atwood et al., 2017; Gunthe et al., 2009; Pöhlker et al., 2016; Rose et al., 2008).
2. Maximum activated fraction of the aerosol population at S: $MAF(S)$
   The fit parameter of CDF, *a(S,D)* gives the ratio of CCN to CN particles at S when 50 % activation has occurred. From this, MAF is calculated as 2**a(S,D)*. If less than 100 % of the aerosol population is activated, MAF will be less than 1 and indicates the presence of externally mixed CCN inactive particles (Gunthe et al., 2009; Pöhlker et al., 2016; Rose et al., 2008).
3. Total number concentration of CCN at S: $N_{CCN}(S)$
   The measured CN distribution was multiplied by the corresponding activation curve or CDF at given S to obtain the CCN distribution. Then, total CCN is calculated by integrating the particles under the CCN number size distribution (Gunthe et al., 2009; Pöhlker et al., 2016; Rose et al., 2008).
4. CCN efficiency of the aerosol population at S: $N_{CCN}(S)/N_{CN}$
   The ratio of total CCN number concentration at a given S to the corresponding total CN number concentration gives the CCN efficiency of the sampled aerosol population (Gunthe et al., 2009; Pöhlker et al., 2016; Rose et al., 2008).

3.7 Aerosol chemical composition and black carbon measurements

Simultaneous measurements of non-refractory PM1 (NR-PM1) aerosols were carried out using an Aerosol Chemical Speciation Monitor (ACSM), which uses a quadrupole mass spectrometer (Ng et al., 2011). The calibration and measurement technique of this instrument are explained in detail elsewhere (Gunthe et al., 2021).

Equivalent mass concentrations of BC ($M_{BC,e}$) were measured using an Aethalometer (Model AE33, MAGEE Scientific). The instrument uses the optical absorption of aerosols at different wavelengths ranging from near infra-red to near ultraviolet to estimate the

mass of BC. The reported $M_{\mathrm{BC,e}}$ corresponds to the optical absorption at 880 nm wavelength. Some of the results and other details of the chemical composition data from these measurements are also reported in Gunthe et al. (2021) and Reyes-Villegas et al. (2020).

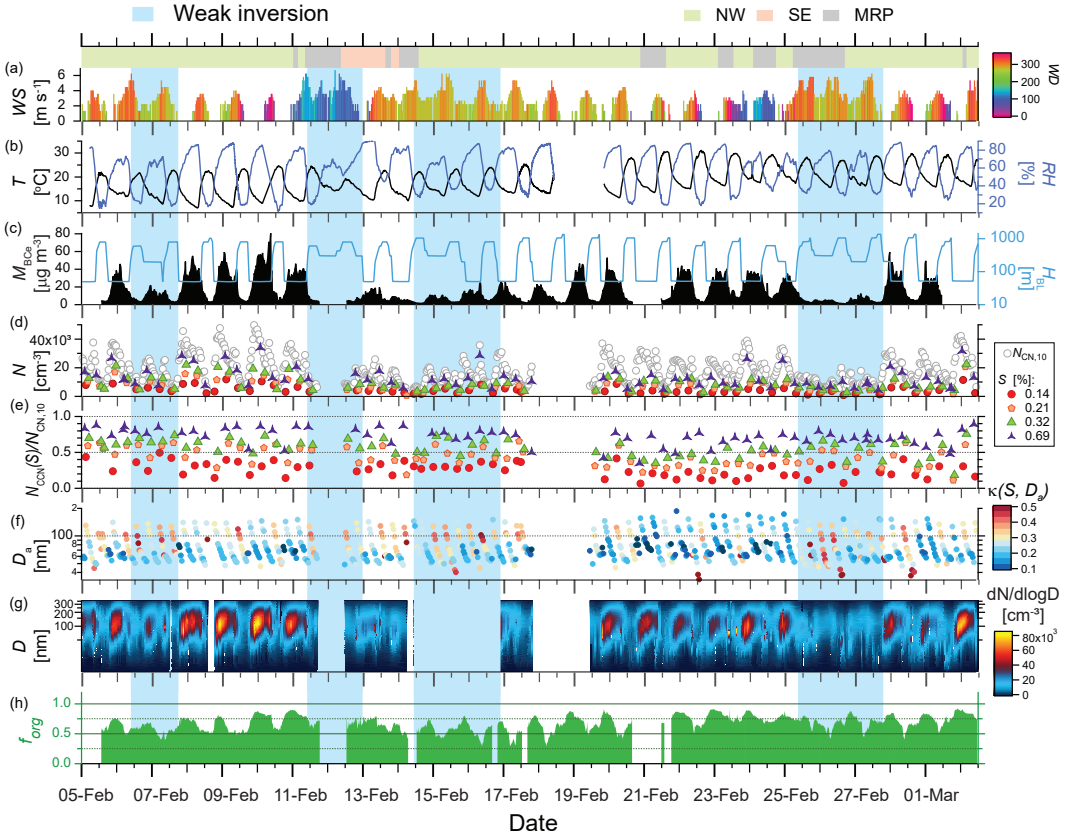

Figure 3. Evolution of meteorological and aerosol parameters shown as a function of local time. Strong radiative inversion periods and weak radiative inversion periods are indicated by white and blue graph background, respectively. The shading on top indicates the air mass observed: north-west (green); south-east (orange) and mixed regional pollution (grey). Temporal evolution of (a): Wind speed (WS, m s^{-1}) colour-scaled by wind direction (WD, degrees); (b): Temperature (T, °C) on the left axis, and relative humidity (RH, %) on the right axis; (c): Mass concentration of equivalent BC ($M_{\mathrm{BC,e}}$, μg m^{-3}) on the left axis, and planetary boundary layer height (H_{BL}, m) from the WRF model on the right axis; (d): Total particle number concentration in the size range ~10 to 370 nm ($N_{\mathrm{CN,10}}$, cm^{-3}), and CCN concentration at selected S levels (N_{CCN}(S), cm^{-3}); (e) CCN efficiency ($N_{\mathrm{CCN}}(S)/N_{\mathrm{CN,10}}$) at selected S levels; (f) Midpoint activation diameter (D_{a}, nm) colour-scaled by corresponding hygroscopicity ($\kappa(S,D_a)$); (g) Particle number size distribution (dN/dlog$D$, cm^{-3}) shown as a heat map from 10 to 370 nm; (h) Organic mass fraction of NR-PM1 (f_{org}).

4 Results and Discussion

An overview of the evolution of Delhi's aerosol and CCN properties along with meteorological parameters observed throughout the campaign is shown as a time series in Figure 3. The top panel of the graph shows the 3-day back trajectory analysis of sampled air masses, using the HYSPLIT model (Stein et al., 2015)(see Sect. 2.2). It shows three distinct directions

in terms of origin and path of the air mass: north-west (NW), south-east (SE) and mixed regional pollution (MRP). Panel (a) shows the wind speed colour-coded by the wind direction (see Sect. 2.1), indicating the occurrence of lower wind speeds during this season on local scale. The wind speed exhibited a systematic diurnal cycle with faster wind during day. The wind direction did not display any diurnal pattern, potentially indicating the influence of surface roughness (Jacobson et al., 2019) on winds in Delhi. The temperature and relative humidity (T and RH, Fig. 3b) cycles diurnally with high T and low RH during day, particularly at late afternoon hours. The alternating occurrence of low wind speed, low T and high RH contributed to significant variations of PBL height (H_{BL}, Fig. 3c), which cycles diurnally and is higher during day.

The evolution of H_{BL} indicates the nocturnal occurrence of a stable atmosphere close to the surface. A strong influence of this low nighttime atmosphere is observed on all measured aerosol properties (Fig. 3c,d,f,g,h). The dependency between H_{BL} and PM1 concentration is in good agreement with previous studies reporting aerosol properties over Delhi (Bhandari et al., 2020; Gani et al., 2019, 2020). In contrast to previous studies, however, we found no correlation between the air mass origin and aerosol properties. This could be attributed to the fact that the effects of air mass origins are manifested in aerosol properties in Delhi only when they originate from another distant and major pollution source such as the stubble burning spots in the neighbouring states of Punjab and Haryana during the crop burning season, predominantly during Oct and Nov (Kulkarni et al., 2020). Such a major pollution event was absent during the campaign (see Sect. 2.2; Gunthe et al. (2021)) and hence the air masses originating from different locations may have not had any strong influence on the locally emitted aerosols within the national capital region. The aerosol properties also did not show any correlation with the evolution of the wind direction. From these observations, we hypothesize that the H_{BL} is the most important meteorological parameter that locally influences aerosol and CCN properties in Delhi, in the absence of any secondary and major source of pollution in the vicinity during the winter season.

To further investigate the dependencies between H_{BL} and characteristic aerosol properties, the diurnal variations of H_{BL}, RH and T along with aerosol properties that show strong correlation to H_{BL} are plotted and shown in Figure 4. We found that the relations between H_{BL} and BC (M_{BCe}, see Fig. 4a and b), and the aerosol loading (see Fig. 4a and b) are the strongest at the diurnal scale. The average diurnal variation of the modelled H_{BL} (Fig. 4a) is in very good agreement with the observed ceilometer data measured at the same location and period as reported by Murthy et al. (2020). An increase in H_{BL} is observed after 07:00 LT (Local Time, i.e. UTC + 05:30) in the morning, corresponding to the rise in temperature and drop in RH. This indicates that the convective mixing after 07:00 LT leads to the breakup of the nocturnal stable layer, resulting in the rise of the mixing layer height higher above the ground, which is sustained until 18:00 LT. As night falls, the ground surface cools faster than the PBL air, causing the radiative inversion and leaving a stable layer relatively close to the ground (Stull, 2012). Hence the nocturnal atmosphere is static, stable, cold and humid, and persisted for an extended duration during nighttime (∼18:00 LT to ∼06:00 LT).

The mass concentration of equivalent BC, the total particle number concentration (Fig. 4b), and the mass concentrations of the NR-PM1 chemical species (Fig. 4c) followed a similar relationship with H_{BL}, indicating a consistent contribution of locally emitted aerosol from sources like fossil fuel combustion, solid biomass burning for domestic cooking and heating, burning of other waste materials, etc. to the aerosol mass burden. All parameters consistently exhibited a morning rush hour peak between 06:00 LT and 08:00 LT, subsequently showing the drop thereafter. This drop strongly coincides with the PBL rise, and therefore can be attributed to dilution by convective mixing. The nighttime peak starts at 19:00 LT and coincides with the evening rush hour and the drop in H_{BL}. Whereas $N_{\mathrm{CN,10}}$ drastically decreased after the rush hour at 21:00 LT, indicating either particle removal or coagulation (to be discussed in follow up studies), the BC and NR-PM1 mass concentrations continued to rise until 01:00 LT. The absolute mass concentration of organic and major inorganic

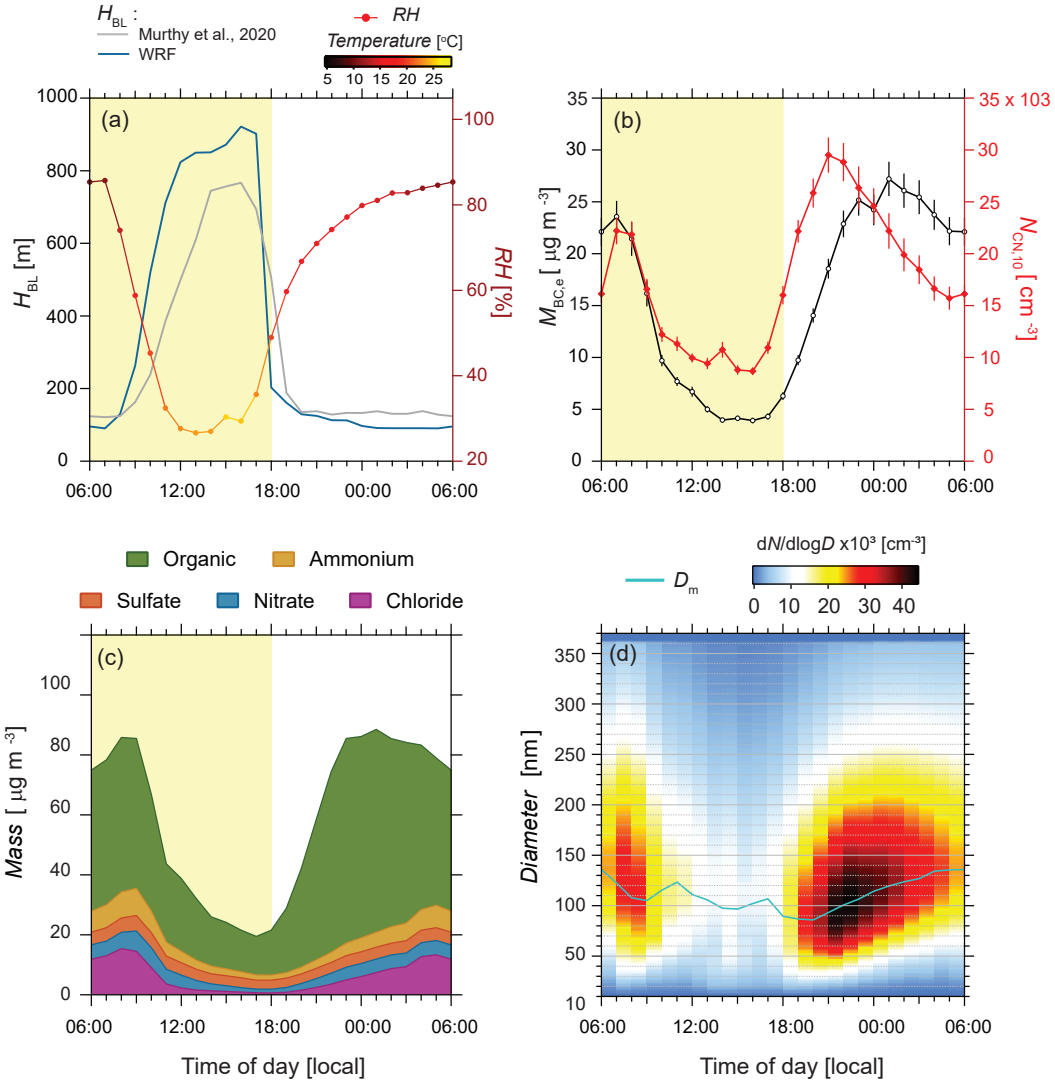

Figure 4. All panels show the campaign-average diurnal variation of the parameters. (a): Planetary boundary layer height (H_{BL}) modeled by the WRF model (blue) and measured by ceilometer from Murthy et al. (2020) (grey) (left axis). The relative humidity, colour scaled by the average diurnal atmospheric temperature, is plotted on the right axis. (b): Equivalent mass of BC ($M_{\mathrm{BC,e}}$) on the left axis and total particle concentration in the size range ∼10 to 370 nm ($N_{\mathrm{CN,10}}$) on the right axis. (c): Mass of NR-PM1 species, organic, ammonium, sulfate, nitrate and chloride from the ACSM as stacked plot. (d): Average size distribution in each hour as a heat map and the modal diameter (D_{m}).

components also followed the typical diurnal trend in concentration variations (Fig. 4c). The prominent late night BC peak has been attributed to diesel engine exhaust emissions from truck and other heavy vehicles, which are permitted passage through Delhi only after 21:00 LT (Guttikunda & Gurjar, 2012). These observations are consistent with PM1 concentrations previously reported by Gani et al. (2019) in Delhi. The average diurnal cycling of aerosol number size distribution (Fig. 4d) further shows that the dominant size range of aerosol particles emitted during the morning and evening rush hours consistently remained in the range of 80 nm to 100 nm. It is interesting to note that a growth in particle

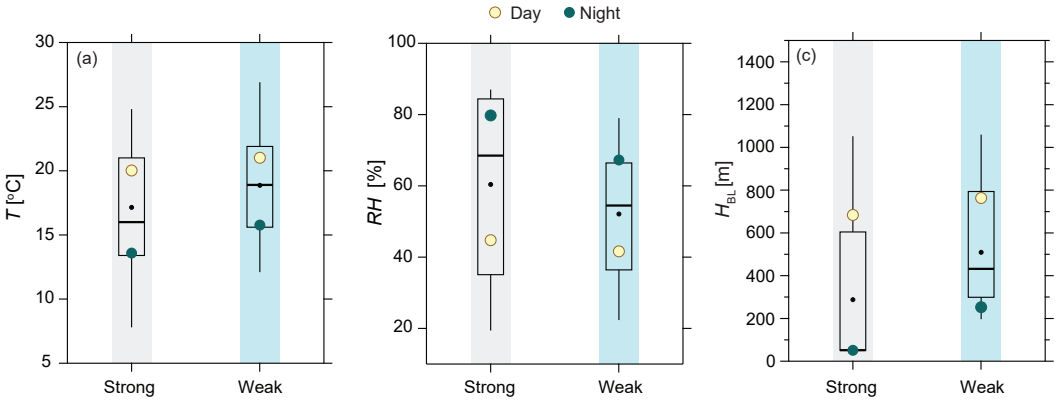

Figure 5. Quartiles and averages of meteorological parameters during strong and weak inversion periods (a): temperature, (b): relative humidity, (c): planetary boundary layer height. The black dots show the averages of all data under the specified period and the other coloured dots show the averages of the data during day and night as given in the figure.

diameter from ∼80 nm to ∼140 nm was observed in modal particle diameter starting from evening hours (18:00 LT) until almost early morning (06:00 LT), consistent with the observations reported by Gani et al. (2020). The detailed mechanism and possible implications of such a growth will be discussed in detail in a follow up study.

With the exception of the CCN efficiency (Fig. 3e), all aerosol and CCN properties exhibited a strong dependence on changes in the local meteorological parameters, particularly the changes in the extent of the temperature inversion and the subsequent variations in H_{BL}. We observed episodes characterized by a larger diurnal variation of T and RH which caused significant variations in H_{BL} diurnally. Contrasting to this, we observed other episodes where the diurnal variation in T and RH were smaller and resulted in smaller variations in H_{BL} diurnally (Fig. 3b). Based on these unique meteorological conditions, these two types of episodes were categorized and further analyses were conducted for these two types: strong inversion periods (Fig. 3, white background: 05 Feb 00:41 to 06 Feb 09:40; 07 Feb 17:39 to 11 Feb 10:02; 12 Feb 23:28 to 14 Feb 10:49; 16 Feb 21:30 to 25 Feb 09:01; 27 Feb 18:50 to 02 Mar 10:39) and weak inversion periods (Fig.3, blue background: 06 Feb 09:41 to 07 Feb 17:38; 11 Feb 10:03 to 12 Feb 23:27; 14 Feb 10:50 to 16 Feb 21:29; 25 Feb 09:02 to 27 Feb 18:49). The diurnal variation of T and RH during strong and weak inversion periods are summarized in Fig. 5a and b. The resulting large diurnal variation of H_{BL} and the extremely low nighttime H_{BL} during strong inversion episodes is shown in contrast to the weaker diurnal variation and higher nighttime H_{BL} during weak inversion episodes in Fig. 5c, consistent with the variations in T and RH. The higher RH during nighttime of strong inversion periods is expected to induce a positive feedback to surface cooling owing to higher heat transfer of moist air (Still et al., 1998) inducing the enhanced atmospheric cooling, which may result in lower PBL height. The detailed correlation between H_{BL} and aerosol and CCN characteristic properties encompassing the two chosen types of periods is shown in Figure 6.

Interestingly, a strong correlation with H_{BL} was exhibited by the averaged PM1 mass concentration ($\mathrm{R}^2 = 0.98$), aerosol number concentration ($\mathrm{R}^2 = 0.95$), and CCN number concentration (N_{CCN}) at various supersaturations ($\mathrm{R}^2 = 0.52$, 0.93 and 0.89 at $S = 0.14\,\%$, $0.32\,\%$ and $0.69\,\%$ respectively). For the average concentrations of characteristic aerosol properties over the entire range of varying H_{BL}, a simple power law fit could provide an extremely effective parameterization. Relatively less strong correlation of N_{CCN} with H_{BL} was observed at $S = 0.14\,\%$, indicating the difficulty in predicting CCN properties at larger particle sizes (∼100 nm; see midpoint activation diameter, D_{a} in Table 1). It

is important to note that the effective relation observed here for use as a possible parameterization is representative of the particular season, local aerosol emissions, and specific meteorological conditions pertaining to this part of the globe. Additional and comprehensive similar measurements over larger spatial areas representing diverse environmental conditions and covering multiple seasons as long-term measurements are very important and must be encouraged as priority to further validate and prove the importance of such a parameterization if used in regional climate models. Nevertheless, the concentration (C) of PM1 mass ($\mu g\,m^{-3}$), and aerosol and CCN number (cm^{-3}) decreases as the power of H_{BL} (m), and can be represented by Equation 1. The resulting fit parameters are summarized in Fig. 6.

$$C = C_{max} * H_{BL}{}^{-p} \tag{1}$$

The parameterization obtained from the correlation fits physically relates to the changes in aerosol concentration resulting from the fluctuations in PBL mixing volume. While the mass concentration decreases as the power of 0.4, the number concentration decreases as the power of 0.3 of H_{BL}.

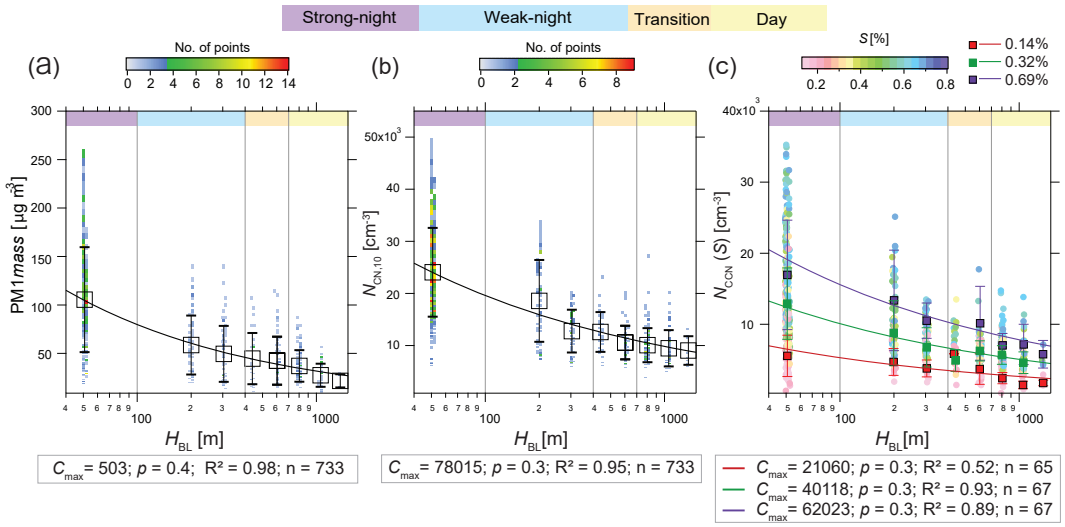

Figure 6. Correlation of H_{BL} with (a): PM1 (b): $N_{CN,10}$, and (c): $N_{CCN}(S)$. The error bars show one standard deviation, and the solid lines show the fit of correlation. The fit parameters and coefficient of determination (R^2) and number of data points (n) are summarized.

The correlations (Fig. 6) also reveal that, as expected, the diurnal variation of aerosol and CCN loading is prominent only during strong inversion periods. To better understand the role of H_{BL} on aerosol properties, processing, and interaction with water vapour, Figure 7 shows various aerosol characteristic properties calculated from measurements for the two distinct boundary layer periods (strong vs. weak) separated for respective day and night times.

A significant difference in aerosol size and hygroscopicity distribution, and chemical composition was observed between day and night during strong inversion periods (Fig. 7a and c). But, such a strong difference was absent during the weak inversion periods indicating that the aerosol characteristic properties remained substantially similar during day and night (Fig. 7b and d). The comparable contribution of BC to PM1 during nighttime under strong and weak inversion periods indicates consistent emissions from similar sources under both episodes. There is also a lack of prominent feedback of aerosols emitted due to increased biofuel use for domestic heating, which one might have expected under low H_{BL}. This is evident from the pronounced variation in aerosol load during night under

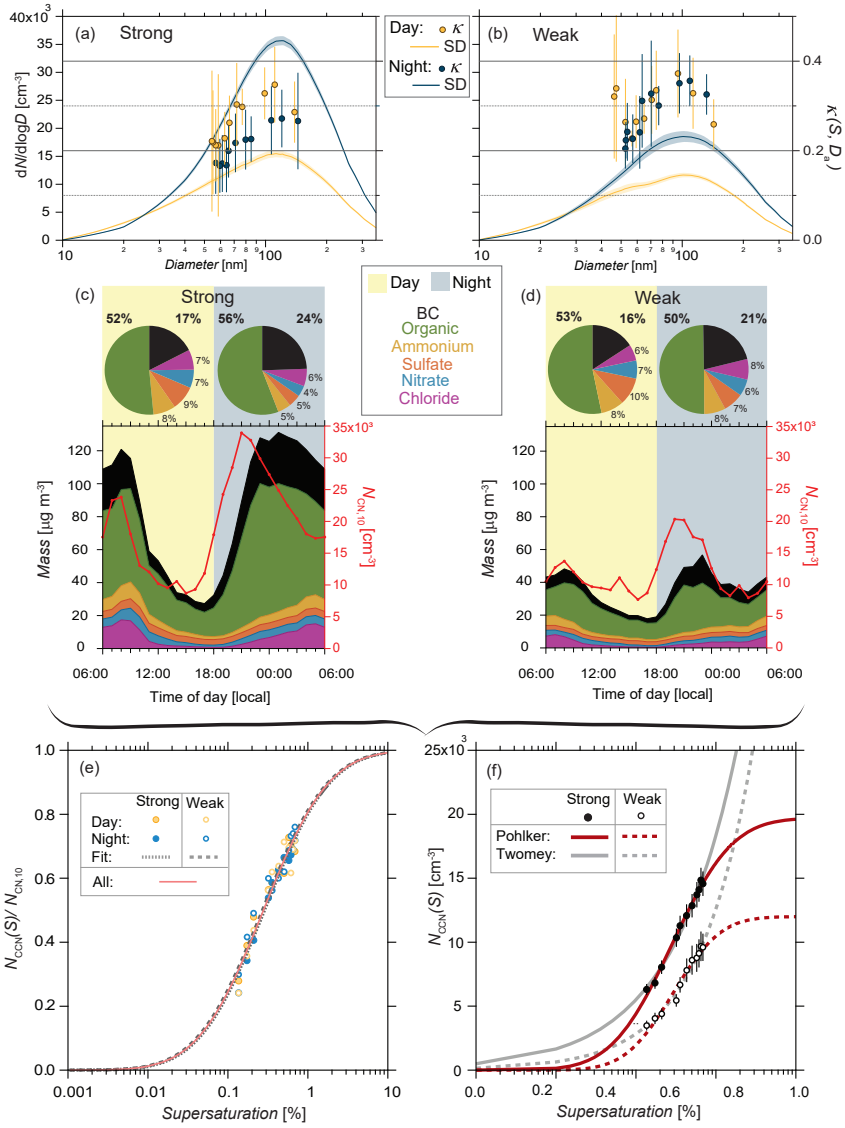

Figure 7. (a): Diurnal average particle number size (left axis) and κ (right axis) distribution during strong inversion periods. The error bars are one standard deviation. (b): Same set of data as shown in (a) for weak inversions. (c): The top panel shows the diurnal average PM1 mass fractions; the bottom panel shows the diurnal average cycle of PM1 mass (left axis) and $N_{\mathrm{CN},10}$ (right axis) under strong inversions (d): Same set of data as in (c) for weak inversions. (e): Single erf-function fit: $y = 0.5 + 0.5$*erf(ln(S/0.28)/2.09) (Pöhlker et al., 2016) on diurnal average data of strong and weak inversions. (f): CCN spectra reproduced using a single erf fit in (e) and measured $N_{\mathrm{CN},10}$ during strong and weak inversions; and the corresponding fits using modified Pöhlker et al. (2016) erf-fit (Eq. 3) and Twomey (1959). The parameters of the modified erf fit of CCN spectra are, strong inversions: $A = 19700\,\mathrm{cm}^{-3}$; $S_{\mathrm{o}} = 0.28\,\%$; $w_{\mathrm{o}} = 1.93$, and weak inversions: $A = 12000\,\mathrm{cm}^{-3}$; $S_{\mathrm{o}} = 0.29\,\%$; $w_{\mathrm{o}} = 1.54$.

strong inversion periods being qualitatively similar to that under weak inversion periods (Fig. 7c and d, $N_{\mathrm{CN},10}$ in grey shaded region), which otherwise is expected to exhibit a consistent aerosol load. However, the lower aerosol hygroscopicity, and high organic

mass fraction during nighttime under strong radiative inversions strongly indicate that aerosol processing and multiphase processes are distinctly different when the PBL is very close to the ground. One of the supporting hypotheses is that freshly emitted organic aerosols possibly undergo rapid chemical transformation and aging under the well mixed layer, whereas the confined boundary layer may inhibit such a transformation and aging. Thus PBL height appears to be the primary factor influencing aerosol formation and chemical processing, followed by emissions, and then further multiphase processes and reactions. This is in contrast to observations from the megacity of Beijing, mainly due to the confined geography of Delhi and the variations in PBL height driven by radiative cooling. This suggests that while aerosol formation and processing over megacities in China (Garland et al., 2009; Li et al., 2020; Rose et al., 2011; T. Su et al., 2020; Tie et al., 2017; Wang et al., 2020; Yu et al., 2020; Zheng et al., 2015) may also be related to PBL height variation, it does not appear to be the primary factor, and the mechanism associated with PBL height variation is different from that in Delhi.

The diurnal CCN efficiencies during both strong and weak inversion periods could be fitted well to a single error function (erf) curve as described by Pöhlker et al. (2016) (Equation 2) (Fig. 7e), which has been applied to measurements at the ATTO site (Andreae et al., 2015), implying that it is not affected by the change in aerosol processing under low H_{BL}.

$$N_{\mathrm{CCN}}(S)/N_{\mathrm{CN,10}} = 0.5 + 0.5 * \mathrm{erf}\left(\frac{\ln(\frac{S}{0.28})}{2.09}\right) \tag{2}$$

This is because the aerosol size distribution during nighttime under strong inversions (very low H_{BL}) had a pronounced accumulation mode (geometric mean diameter $\sim$132 nm). Therefore, the abundance of bigger particles overrides the effect of reduced hygroscopicity, yielding similar CCN efficiency spectra, once again reinforcing that size matters more than chemistry for the activation of the CCN, consistent with previous studies (Dusek et al. (2006); Gunthe et al. (2009, 2011) and references therein). Moreover, the high CCN efficiency achieved at maximum measured $S = 0.69\,\%$ during both strong and weak inversions (70 % and 74 % respectively) is comparable with the contrastingly near-pristine Amazon rain forest (78 % at S=0.61 %; Pöhlker et al. (2016)), and also verifies the high activated fractions estimated by Arub et al. (2020). The combined CCN efficiency spectrum is used with the measured total particle concentration of strong and weak inversion periods to reproduce the CCN spectra (Fig. 7f, black dots and circles respectively). The sensitivity of CCN to H_{BL} is captured well using the single CCN parameterization. The modified erf fit for CCN spectra (Equation 3) based on Pöhlker et al. (2016) represents the CCN spectra physically much better than the traditional Twomey power law fit (Twomey, 1959), by converging against corresponding $N_{\mathrm{CN,10}}$ at high S. The fit parameters of CCN spectra under strong and weak inversion periods are summarized in the caption of Fig. 7.

$$N_{\mathrm{CCN}}(S) = A/2 + A/2 * \mathrm{erf}\left(\frac{\ln(\frac{S}{S_{\mathrm{o}}})}{w_{\mathrm{o}}}\right) \tag{3}$$

The modified erf fit of the CCN spectra converges to A, which is in good agreement with the $N_{\mathrm{CN,10}}$ under the different meteorological conditions. This effectively shows that the combined CCN efficiency spectra are sufficient for modelling CCN activity using total aerosol load under varying meteorological conditions.

5 Summary

From our comprehensive investigation of aerosol and CCN in Delhi we found that the PBL height plays an important role in modulating aerosol and CCN properties, which can be well explained using simple parameterizations. The pronounced diurnal variation

of aerosol loading during the strong radiative inversion periods with similar emissions supports the hypothesis that H_{BL} is the major factor affecting aerosol processing in Delhi. We suggest that the distinct meteorological processes in the confined and poorly ventilated Delhi air basin are starkly different from other megacities in the world and may enhance the significance of H_{BL} in modulating CCN activation and other multiphase processes. We present the set of parameterizations encompassing the correlation of PM1 mass, aerosol and CCN number concentrations to H_{BL}, and CCN activity obtained from field observations.

The origin of the air masses did not show any influence on the aerosols, since they come from relatively less polluted regions than the local surroundings in the extremely polluted megacity. Only during the crop residue burning season (Oct and Nov) is there another major pollution source outside the megacity. In the absence of this source in the late winter, the surrounding regions do not significantly affect the aerosol properties in Delhi. The local wind direction also had no effect on aerosols, implying that the measured aerosol and CCN properties are representative of the metropolitan area.

The H_{BL} correlated most strongly with the aerosol and CCN number concentrations, and PM1 mass concentrations. These characteristic aerosol properties decreased as a power function of H_{BL}. The aerosol hygroscopicity however, was less affected by the H_{BL} and was lower during times of low H_{BL}. This change in hygroscopicity under nearly the same emission scenario leads to the hypothesis that aerosol processing is influenced by H_{BL}. The dependence on H_{BL} also leads to a diurnal cycle of aerosol properties, which was pronounced under strong radiative inversion conditions. Such a feature appears to be very specific to Delhi, making it markedly distinct from other polluted megacities in the world, including Beijing (Gunthe et al., 2021).

Regardless of the change in aerosol number and chemistry by the strong variations in H_{BL}, the CCN efficiencies were not affected and remained consistent for the whole measurement period. Hence a single parameterization could model the CCN activity and captured the variability in CCN concentration under varying meteorological conditions. The CCN spectrum is well represented by the error function fit (Equation 2; Pöhlker et al. (2016)) and the modified Pöhlker et al. (2016) error function fit (Equation 3).

Our study shows that the interplay between aerosol and water vapour leading to CCN number variability in the polluted atmosphere of Delhi primarily depends on the unique local meteorology, and that the PBL contains abundant efficient CCN, which can readily activate as cloud droplets. Since very high aerosol and CCN concentrations are contained within the extremely low PBL, it could lead to fog and haze formation adversely affecting air quality and public health. Moreover, the elevated CCN particles could enter clouds and contribute to cloud microphysical effects (Stocker et al., 2013), implying changes to the aerosol-cloud interaction radiative forcing in Delhi. Our findings are expected to improve the representation of aerosols and CCN activity particularly over the Indian region, where accurate measurements are in sparse. This would help to formulate control measures for improving regional air quality and mitigating public health impacts. More measurements under varying environmental conditions for longer duration are urgently required for validation and further improvement of the proposed parameterization covering the entire Indian sub-continent. It is important to note that the interaction between meteorology and aerosol properties presented here is specific to the location and season of the year. Since aerosol properties are dynamic in nature, further measurements are strongly encouraged over the Indian subcontinent under contrasting environments and during other seasons.

Acknowledgments

SSG gratefully acknowledges funding from Ministry of Earth Sciences (MoES; sanction number MoES/16/20/12-RDEAS dated 31.Mar.2014), Government of India, for the purchase of the Cloud Condensation Nuclei Counter (CCNC). This work was supported by partial funding from the Ministry of Earth Sciences (MoES; sanction number MoES/16/04/2017-APHH (PROMOTE)), Government of India. This work was also partially supported by the UK Natural Environment Research Council and the Newton Fund through the PROMOTE project of the APHH-Delhi programme, grant ref. NE/P016480/1 and NE/P016472/1.

All the authors are grateful to the APHH-PROMOTE team for providing logistic and experimental support during the campaign. We thank Alfatech Services, New Delhi, for their generous technical support during the campaign. SSR was the recipient of a scholarship from the Indo-German Centre for Sustainability through the German Academic Exchange Service under the initiative 'A New Passage to India' funded through the Federal Ministry for Education and Research in 2019 and 2020. SSR, MLP and SSG acknowledge this support for conducting in-person and virtual discussions. SSR acknowledges the team at Max Planck Institute for Chemistry for facilitating the research stay and discussions. SSR also acknowledges the Ministry of Human Resources Development, Government of India for a fellowship.

The data associated with key results have been deposited in associated data files in an open research repository. The time series of corrected data from size-resolved CCN experiments with modelled PBL height (named "CCN.dat"); time series of inverted particle number size distribution (named "SD.dat"); and campaign average of CCN properties (named "AvgCCN.dat") are available in NASA Ames format under https://dx.doi.org/10.17617/3.5y (Raj et al., 2021).

Author Contribution

SSG conceived the idea and designed the research. SSG, GM, and HC conceptualized and planned the field measurement campaign. SSR led the logistic planning and execution of the field campaign. SSR, AS, U. Panda, ED, and SS, carried out robust calibrations and extensive field measurements and collected CCN and ACSM data. MLP and SSR led the CCN data analysis with help from TK. SSR led the size data inversion with help from TK and MLP. SSR led the back trajectory data analysis with help from DW, J-DF, and CP. SSR led the fire spot analysis with help from DW and OK. U. Panda and JA carried out the ACSM data analysis. SSR, MLP, and SSG led the CCN data interpretation with inputs from OK and RR. SSG, RR, U. Panda and SSR led the ACSM data interpretation with inputs from JA, GM, and HC. VKS and RPS provided meteorological data and SSR led the interpretation. SSR wrote the first draft of the manuscript under the mentorship of SSG, with critical edits and inputs form MLP, and comments from STM, U. Pöschl, and MOA. All the co-authors discussed the results and commented on the manuscript.

References

Andreae, M. O., Acevedo, O. C., Araùjo, A., Artaxo, P., Barbosa, C. G. G., Barbosa, H. M. J., Brito, J., Carbone, S., Chi, X., Cintra, B. B. L., da Silva, N. F., Dias, N. L., Dias-Júnior, C. Q., Ditas, F., Ditz, R., Godoi, A. F. L., Godoi, R. H. M., Heimann, M., Hoffmann, T., Kesselmeier, J., Könemann, T., Krüger, M. L., Lavric, J. V., Manzi, A. O., Lopes, A. P., Martins, D. L., Mikhailov, E. F., Moran-Zuloaga, D., Nelson, B. W., Nölscher, A. C., Santos Nogueira, D., Piedade, M. T. F., Pöhlker, C., Pöschl, U., Quesada, C. A., Rizzo, L. V., Ro, C.-U., Ruckteschler, N., Sá, L. D. A., de Oliveira Sá, M., Sales, C. B., dos Santos, R. M. N., Saturno, J., Schöngart, J., Sörgel, M., de Souza, C. M., de Souza, R. A. F., Su, H., Targhetta, N., Tóta, J., Trebs, I., Trumbore, S., van Eijck, A., Walter, D., Wang, Z., Weber, B., Williams, J., Winderlich, J., Wittmann, F., Wolff, S., & Yáñez Serrano, A. M. (2015). The Amazon Tall Tower Observatory (ATTO): overview of pilot measurements on ecosystem ecology, meteorology, trace gases, and aerosols. *Atmospheric Chemistry and Physics*, *15*(18), 10723–10776. doi: 10.5194/acp-15-10723-2015

Arub, Z., Bhandari, S., Gani, S., Apte, J. S., Hildebrandt Ruiz, L., & Habib, G. (2020). Air mass physiochemical characteristics over New Delhi: impacts on aerosol hygroscopicity and cloud condensation nuclei (CCN) formation. *Atmospheric Chemistry and Physics*, *20*(11), 6953–6971. doi: 10.5194/acp-20-6953-2020

Arun, S. H., Sharma, S. K., Chaurasia, S., Vaishnav, R., & Kumar, R. (2018).

Fog/low clouds detection over the Delhi Earth Station using the Ceilometer and the INSAT-3D/3DR satellite data. *International Journal of Remote Sensing*, *39*(12), 4130–4144. doi: 10.1080/01431161.2018.1454624

Asa-Awuku, A., Sorooshian, A., Flagan, R. C., Seinfeld, J. H., & Nenes, A. (2015). CCN properties of organic aerosol collected below and within marine stratocumulus clouds near Monterey, California. *Atmosphere*, *6*(11), 1590–1607. doi: 10.3390/atmos6111590

Atwood, S. A., Reid, J. S., Kreidenweis, S. M., Blake, D. R., Jonsson, H. H., Lagrosas, N. D., Xian, P., Reid, E. A., Sessions, W. R., & Simpas, J. B. (2017). Size-resolved aerosol and cloud condensation nuclei (CCN) properties in the remote marine South China Sea–Part 1: Observations and source classification. *Atmospheric Chemistry and Physics*, *17*(2), 1105–1123. doi: 10.5194/acp-17-1105-2017

Bhandari, S., Gani, S., Patel, K., Wang, D. S., Soni, P., Arub, Z., Habib, G., Apte, J. S., & Hildebrandt Ruiz, L. (2020). Sources and atmospheric dynamics of organic aerosol in New Delhi, India: insights from receptor modelling. *Atmospheric Chemistry and Physics*, *20*(2), 735–752. doi: 10.5194/acp-20-735-2020

Bhattu, D., Tripathi, S. N., & Chakraborty, A. (2016). Deriving aerosol hygroscopic mixing state from size-resolved CCN activity and HR-ToF-AMS measurements. *Atmospheric Environment*, *142*, 57–70. doi: 10.1016/j.atmosenv.2016.07.032

Boucher, O., Randall, D., Artaxo, P., Bretherton, C., Feingold, G., Forster, P., Kerminen, V.-M., Kondo, Y., Liao, H., Lohmann, U., Rasch, P., Satheesh, S., Sherwood, S., Stevens, B., & Zhang, X. (2013). Cloud and Aerosols. In: *Climate Change 2013: The Physical Science Basis. Contribution of Working Group I to the Fifth Assessment Report of the Intergovernmental Panel on Climate Change* [Stocker, T.F., D. Qin, G.-K. Plattner, M. Tignor, S.K. Allen, J. Boschung, A. Nauels, Y. Xia, V. Bex and P.M. Midgley (eds.)]. *Cambridge University Press, Cambridge, United Kingdom and New York, NY, USA.*

Che, H. C., Zhang, X. Y., Zhang, L., Wang, Y. Q., Zhang, Y. M., Shen, X. J., Ma, Q. L., Sun, J. Y., & Zhong, J. T. (2017). Prediction of size-resolved number concentration of cloud condensation nuclei and long-term measurements of their activation characteristics. *Scientific Reports*, *7*(1), 1–12. doi: 10.1038/s41598-017-05998-3

Cheng, Y., Zheng, G., Wei, C., Mu, Q., Zheng, B., Wang, Z., Gao, M., Zhang, Q., He, K., Carmichael, G., Pöschl, U., & Su, H. (2016). Reactive nitrogen chemistry in aerosol water as a source of sulfate during haze events in China. *Science Advances*, *2*(12), e1601530. doi: 10.1126/sciadv.1601530

Dumka, U. C., Tiwari, S., Kaskaoutis, D. G., Soni, V. K., Safai, P. D., & Attri, S. D. (2019). Aerosol and pollutant characteristics in Delhi during a winter research campaign. *Environmental Science and Pollution Research*, *26*(4), 3771–3794. doi: 10.1007/s11356-018-3885-y

Dusek, U., Frank, G. P., Hildebrandt, L., Curtius, J., Schneider, J., Walter, S., Chand, D., Drewnick, F., Hings, S., Jung, D., Borrmann, S., & Andreae, M. O. (2006). Size matters more than chemistry for cloud-nucleating ability of aerosol particles. *Science*, *312*(5778), 1375–1378. doi: 10.1126/science.1125261

Frank, G. P., Dusek, U., & Andreae, M. O. (2006). Technical note: A method for measuring size-resolved ccn in the atmosphere. *Atmospheric Chemistry and Physics Discussions*, *6*, 4879–4895. doi: 10.5194/acpd-6-4879-2006

Gani, S., Bhandari, S., Patel, K., Seraj, S., Soni, P., Arub, Z., Habib, G., Hildebrandt Ruiz, L., & Apte, J. S. (2020). Particle number concentrations and size distribution in a polluted megacity: the Delhi Aerosol Supersite study. *Atmospheric Chemistry and Physics*, *20*(14), 8533–8549. doi: 10.5194/acp-20-8533-2020

Gani, S., Bhandari, S., Seraj, S., Wang, D. S., Patel, K., Soni, P., Arub, Z., Habib, G., Hildebrandt Ruiz, L., & Apte, J. S. (2019). Submicron aerosol composition in the world's most polluted megacity: the Delhi Aerosol Supersite study. *Atmospheric Chemistry and Physics*, *19*(10), 6843–6859. doi: 10.5194/acp-19-6843-2019

Garland, R. M., Schmid, O., Nowak, A., Achtert, P., Wiedensohler, A., Gunthe, S. S., Takegawa, N., Kita, K., Kondo, Y., Hu, M., Shao, M., Zeng, L. M., Zhu, T., Andreae, M. O., & Pöschl, U. (2009). Aerosol optical properties observed during Campaign of Air Quality Research in Beijing 2006 (CAREBeijing-2006): Characteristic differences between the inflow and outflow of Beijing city air. *Journal of Geophysical Research: Atmospheres*, *114*(D2). doi: 10.1029/2008JD010780

Garyfallidis, E., Brett, M., Correia, M. M., Williams, G. B., & Nimmo-Smith, I. (2012). Quickbundles, a method for tractography simplification. *Frontiers in Neuroscience*, *6*, 175. doi: 10.3389/fnins.2012.00175

Gunn, R. (1954). Diffusion Charging of Atmospheric Droplets by Ions, and the Resulting Combination Coefficients. *Journal of Atmospheric Sciences*, *11*(5), 339-347. doi: 10.1175/1520-0469(1954)011⟨0339:DCOADB⟩2.0.CO;2

Gunthe, S. S., King, S. M., Rose, D., Chen, Q., Roldin, P., Farmer, D. K., Jimenez, J. L., Artaxo, P., Andreae, M. O., Martin, S. T., & Pöschl, U. (2009). Cloud condensation nuclei in pristine tropical rainforest air of Amazonia: size-resolved measurements and modelling of atmospheric aerosol composition and CCN activity. *Atmospheric Chemistry and Physics*, *9*(19), 7551–7575. doi: 10.5194/acp-9-7551-2009

Gunthe, S. S., Liu, P., Panda, U., Raj, S. S., Sharma, A., Darbyshire, E., Reyes-Villegas, E., Allan, J., Chen, Y., Wang, X., Song, S., Pöhlker, M. L., Shi, L., Wang, Y., Kommula, S. M., Liu, T., Ravikrishna, R., McFiggans, G., Mickley, L. J., Martin, S. T., Pöschl, U., Andreae, M. O., & Coe, H. (2021). Enhanced aerosol particle growth sustained by high continental chlorine emission in India. *Nature Geoscience*, *14*(2), 77–84. doi: 10.1038/s41561-020-00677-x

Gunthe, S. S., Rose, D., Su, H., Garland, R. M., Achtert, P., Nowak, A., Wiedensohler, A., Kuwata, M., Takegawa, N., Kondo, Y., Hu, M., Shao, M., Zhu, T., Andreae, M. O., & Pöschl, U. (2011). Cloud condensation nuclei (CCN) from fresh and aged air pollution in the megacity region of Beijing. *Atmospheric Chemistry and Physics*, *11*(21), 11023–11039. doi: 10.5194/acp-11-11023-2011

Guttikunda, S. K., & Calori, G. (2013). A GIS based emissions inventory at 1 km× 1 km spatial resolution for air pollution analysis in Delhi, India. *Atmospheric Environment*, *67*, 101–111. doi: 10.1016/j.atmosenv.2012.10.040

Guttikunda, S. K., & Gurjar, B. R. (2012). Role of meteorology in seasonality of air pollution in megacity Delhi, India. *Environmental Monitoring and Assessment*, *184*(5), 3199–3211. doi: 10.1007/s10661-011-2182-8

Henning, S., Dieckmann, K., Ignatius, K., Schäfer, M., Zedler, P., Harris, E., Sinha, B., van Pinxteren, D., Mertes, S., Birmili, W., Merkel, M., Wu, Z., Wiedensohler, A., Wex, H., Herrmann, H., & Stratmann, F. (2014). Influence of cloud processing on CCN activation behaviour in the Thuringian Forest, Germany during HCCT-2010. *Atmospheric Chemistry and Physics*, *14*(15), 7859–7868. doi: 10.5194/acp-14-7859-2014

Iwamoto, Y., Kinouchi, K., Watanabe, K., Yamazaki, N., & Matsuki, A. (2016). Simultaneous measurement of CCN activity and chemical composition of fine-mode aerosols at Noto peninsula, Japan, in autumn 2012. *Aerosol and Air Quality Research*, *16*(9), 2107–2118. doi: 10.4209/aaqr.2015.09.0545

Jacobson, M. Z., Nghiem, S. V., & Sorichetta, A. (2019). Short-Term Impacts of the Megaurbanizations of New Delhi and Los Angeles Between 2000 and

2009. *Journal of Geophysical Research: Atmospheres*, *124*(1), 35–56. doi: 10.1029/2018JD029310

Jain, M., Dawa, D., Mehta, R., Dimri, A., & Pandit, M. (2016). Monitoring land use change and its drivers in Delhi, India using multi-temporal satellite data. *Modelling Earth Systems and Environment*, *2*(1), 19. doi: 10.1007/s40808-016-0075-0

Jaiprakash, A., Singhai, Habib, G., Raman, R. S., & Gupta, T. (2017). Chemical characterization of PM 1.0 aerosol in Delhi and source apportionment using positive matrix factorization. *Environmental Science and Pollution Research*, *24*(1), 445–462. doi: 10.1007/s11356-016-7708-8

Jayachandran, V. N., Babu, S. N. S., Vaishya, A., Gogoi, M. M., Nair, V. S., Satheesh, S. K., & Moorthy, K. K. (2020). Altitude profiles of cloud condensation nuclei characteristics across the Indo-Gangetic Plain prior to the onset of the Indian summer monsoon. *Atmospheric Chemistry and Physics*, *20*(1), 561–576. doi: 10.5194/acp-20-561-2020

Knutson, E., & Whitby, K. (1975). Aerosol classification by electric mobility: apparatus, theory, and applications. *Journal of Aerosol Science*, *6*(6), 443-451. doi: 10.1016/0021-8502(75)90060-9

Kulkarni, S. H., Ghude, S. D., Jena, C., Karumuri, R. K., Sinha, B., Sinha, V., Kumar, R., Soni, V. K., & Khare, M. (2020). How much does large-scale crop residue burning affect the air quality in delhi? *Environmental Science & Technology*, *54*(8), 4790–4799. doi: 10.1021/acs.est.0c00329

Kumar, N., Soni, K., Garg, N., Agarwal, R., Saha, D., Singh, M., & Singh, G. (2017). SODAR pattern classification and its dependence on meteorological parameters over a semiarid region of India. *International Journal of Remote Sensing*, *38*(11), 3466–3482. doi: 10.1080/01431161.2017.1294774

Lelieveld, J., Pozzer, A., Pöschl, U., Fnais, M., Haines, A., & Münzel, T. (2020). Loss of life expectancy from air pollution compared to other risk factors: a worldwide perspective. *Cardiovascular Research*, *116*(11), 1910–1917. doi: 10.1093/cvr/cvaa025

Li, G., Su, H., Ma, N., Tao, J., Kuang, Y., Wang, Q., Hong, J., Zhang, Y., Kuhn, U., Zhang, S., Pan, X., Lu, N., Tang, M., Zheng, G., Wang, Z., Gao, Y., Cheng, P., Xu, W., Zhou, G., Zhao, C., Yuan, B., Shao, M., Ding, A., Zhang, Q., Fu, P., Sun, Y., Pöschl, U., & Cheng, Y. (2020). Multiphase chemistry experiment in Fogs and Aerosols in the North China Plain (McFAN): integrated analysis and intensive winter campaign 2018. *Faraday Discussions*. doi: 10.1039/D0FD00099J

Ma, Y., Li, S., Zheng, J., Khalizov, A., Wang, X., Wang, Z., & Zhou, Y. (2017). Size-resolved measurements of mixing state and cloud-nucleating ability of aerosols in Nanjing, China. *Journal of Geophysical Research: Atmospheres*, *122*(17), 9430–9450. doi: 10.1002/2017JD026583

Mandal, P., Sarkar, R., Mandal, A., & Saud, T. (2014). Seasonal variation and sources of aerosol pollution in Delhi, India. *Environmental Chemistry Letters*, *12*(4), 529–534. doi: 10.1007/s10311-014-0479-x

Murthy, B., Latha, R., Tiwari, A., Rathod, A., Singh, S., & Beig, G. (2020). Impact of mixing layer height on air quality in winter. *Journal of Atmospheric and Solar-Terrestrial Physics*, *197*, 105157. doi: 10.1016/j.jastp.2019.105157

Ng, N. L., Herndon, S. C., Trimborn, A., Canagaratna, M. R., Croteau, P. L., Onasch, T. B., Sueper, D., Worsnop, D. R., Zhang, Q., Sun, Y. L., & Jayne, J. T. (2011). An Aerosol Chemical Speciation Monitor (ACSM) for routine monitoring of the composition and mass concentrations of ambient aerosol. *Aerosol Science and Technology*, *45*(7), 780–794. doi: 10.1080/02786826.2011.560211

Ojha, N., Sharma, A., Kumar, M., Girach, I., Ansari, T. U., Sharma, S. K., Singh, N., Pozzer, A., & Gunthe, S. S. (2020). On the widespread enhancement

in fine particulate matter across the Indo-Gangetic Plain towards winter. *Scientific Reports*, *10*(1), 1–9. doi: 10.1038/s41598-020-62710-8

Paul, S., Saxena, K. G., Nagendra, H., & Lele, N. (2021). Tracing land use and land cover change in peri-urban Delhi, India, over 1973–2017 period. *Environmental Monitoring and Assessment*, *193*(2), 1–12. doi: 10.1007/s10661-020-08841-x

Petters, M., & Kreidenweis, S. (2007). A single parameter representation of hygroscopic growth and cloud condensation nucleus activity. *Atmospheric Chemistry and Physics*, *7*(8), 1961–1971. doi: 10.5194/acp-7-1961-2007

Pöhlker, M. L., Ditas, F., Saturno, J., Klimach, T., Hrabě de Angelis, I., Araùjo, A. C., Brito, J., Carbone, S., Cheng, Y., Chi, X., Ditz, R., Gunthe, S. S., Holanda, B. A., Kandler, K., Kesselmeier, J., Könemann, T., Krüger, O. O., Lavrič, J. V., Martin, S. T., Mikhailov, E., Moran-Zuloaga, D., Rizzo, L. V., Rose, D., Su, H., Thalman, R., Walter, D., Wang, J., Wolff, S., Barbosa, H. M. J., Artaxo, P., Andreae, M. O., Pöschl, U., & Pöhlker, C. (2018). Long-term observations of cloud condensation nuclei over the Amazon rain forest–Part 2: Variability and characteristics of biomass burning, long-range transport, and pristine rain forest aerosols. *Atmospheric Chemistry and Physics*, *18*(14), 10289–10331. doi: 10.5194/acp-18-10289-2018

Pöhlker, M. L., Pöhlker, C., Ditas, F., Klimach, T., Hrabe de Angelis, I., Araújo, A., Brito, J., Carbone, S., Cheng, Y., Chi, X., Ditz, R., Gunthe, S. S., Kesselmeier, J., Könemann, T., Lavrič, J. V., Martin, S. T., Mikhailov, E., Moran-Zuloaga, D., Rose, D., Saturno, J., Su, H., Thalman, R., Walter, D., Wang, J., Wolff, S., Barbosa, H. M. J., Artaxo, P., Andreae, M. O., & Pöschl, U. (2016). Long-term observations of cloud condensation nuclei in the Amazon rain forest–Part 1: Aerosol size distribution, hygroscopicity, and new model parametrizations for CCN prediction. *Atmospheric Chemistry and Physics*, *16*(24), 15709–15740. doi: 10.5194/acp-16-15709-2016

Raatikainen, T., Hyvärinen, A.-P., Hatakka, J., Panwar, T., Hooda, R., Sharma, V., & Lihavainen, H. (2011). Comparison of aerosol properties from the Indian Himalayas and the Indo-Gangetic plains. *Atmospheric Chemistry and Physics Discussions*, *11*(4), 11417–11453. doi: 10.1016/j.atmosenv.2014.02.058

Raj, S. S., Pöhlker, M., Sharma, A., & Gunthe, S. S. (2021). Delhi size-resolved CCN, PBL and SD data in Raj et al. 2021. *Max Planck Society*. doi: 10.17617/3.5y

Reyes-Villegas, E., Panda, U., Darbyshire, E., Cash, J. M., Joshi, R., Langford, B., Di Marco, C. F., Mullinger, N., Acton, W. J. F., Drysdale, W., Nemitz, E., Flynn, M., Voliotis, A., McFiggans, G., Coe, H., Lee, J., Hewitt, C. N., Heal, M. R., Gunthe, S. S., Shivani, Gadi, R., Singh, S., Soni, V., & Allan, J. D. (2020). PM 1 composition and source apportionment at two sites in Delhi, India across multiple seasons. *Atmospheric Chemistry and Physics Discussions*, 1–19. doi: 10.5194/acp-2020-894

Roberts, G. C., & Nenes, A. (2005). A continuous-flow streamwise thermal-gradient CCN chamber for atmospheric measurements. *Aerosol Science and Technology*, *39*(3), 206–221. doi: 10.1080/027868290913988

Rose, D., Gunthe, S. S., Mikhailov, E., Frank, G., Dusek, U., Andreae, M. O., & Pöschl, U. (2008). Calibration and measurement uncertainties of a continuous-flow cloud condensation nuclei counter (DMT-CCNC): CCN activation of ammonium sulfate and sodium chloride aerosol particles in theory and experiment. *Atmospheric Chemistry and Physics*, *8*(5), 1153–1179. doi: 10.5194/acp-8-1153-2008

Rose, D., Gunthe, S. S., Su, H., Garland, R. M., Yang, H., Berghof, M., Cheng, Y. F., Wehner, B., Achtert, P., Nowak, A., Wiedensohler, A., Takegawa, N., Kondo, Y., Hu, M., Zhang, Y., Andreae, M. O., & Pöschl, U. (2011). Cloud condensation nuclei in polluted air and biomass burning smoke near the mega-city Guangzhou, China–Part 2: Size-resolved aerosol chemical

composition, diurnal cycles, and externally mixed weakly CCN-active soot particles. *Atmospheric Chemistry and Physics*, *11*(6), 2817–2836. doi: 10.5194/acp-11-2817-2011

Rose, D., Nowak, A., Achtert, P., Wiedensohler, A., Hu, M., Shao, M., Zhang, Y., Andreae, M. O., & Pöschl, U. (2010). Cloud condensation nuclei in polluted air and biomass burning smoke near the mega-city Guangzhou, China–Part 1: Size-resolved measurements and implications for the modelling of aerosol particle hygroscopicity and CCN activity. *Atmospheric Chemistry and Physics*, *10*(7), 3365–3383. doi: 10.5194/acp-10-3365-2010

Stein, A. F., Draxler, R. R., Rolph, G. D., Stunder, B. J. B., Cohen, M. D., & Ngan, F. (2015). NOAA's HYSPLIT atmospheric transport and dispersion modelling system. *Bulletin of the American Meteorological Society*, *96*(12), 2059–2077. doi: 10.1175/BAMS-D-14-00110.1

Still, M., Venzke, H., Durst, F., & Melling, A. (1998). Influence of humidity on the convective heat transfer from small cylinders. *Experiments in Fluids*, *24*(2), 141–150. doi: 10.1007/s003480050161

Stocker, T., Qin, D., Plattner, G.-K., Tignor, M., Allen, S., Boschung, J., Nauels, A., Xia, Y., Bex, V., Midgley, P., & (eds.). (2013). IPCC, 2013: Climate Change 2013: The Physical Science Basis. Contribution of Working Group I to the Fifth Assessment Report of the Intergovernmental Panel on Climate Change. *Cambridge University Press, Cambridge, United Kingdom and New York, NY, USA*.

Stull, R. B. (2012). *An introduction to boundary layer meteorology* (Vol. 13). Springer Science & Business Media.

Su, H., Cheng, Y., & Pöschl, U. (2020). New Multiphase Chemical Processes Influencing Atmospheric Aerosols, Air Quality, and Climate in the Anthropocene. *Accounts of Chemical Research*, *53*(10), 2034–2043. doi: 10.1021/acs.accounts.0c00246

Su, T., Li, Z., Zheng, Y., Luan, Q., & Guo, J. (2020). Abnormally shallow boundary layer associated with severe air pollution during the COVID-19 lockdown in China. *Geophysical Research Letters*, *47*(20), e2020GL090041. doi: 10.1029/2020GL090041

Thomas, A., Sarangi, C., & Kanawade, V. P. (2019). Recent increase in winter hazy days over Central India and the Arabian Sea. *Scientific Reports*, *9*(1), 1–10. doi: 10.1038/s41598-019-53630-3

Tie, X., Huang, R.-J., Cao, J., Zhang, Q., Cheng, Y., Su, H., Chang, D., Pöschl, U., Hoffmann, T., Dusek, U., Li, G., Worsnop, D. R., & O'Dowd, C. D. (2017). Severe pollution in China amplified by atmospheric moisture. *Scientific Reports*, *7*(1), 1–8. doi: 10.1038/s41598-017-15909-1

Tiwari, S., Srivastava, A. K., Bisht, D. S., Parmita, P., Srivastava, M. K., & Attri, S. (2013). Diurnal and seasonal variations of black carbon and PM2. 5 over New Delhi, India: Influence of meteorology. *Atmospheric Research*, *125*, 50–62. doi: 10.1016/j.atmosres.2013.01.011

Twomey, S. (1959). The nuclei of natural cloud formation part II: The supersaturation in natural clouds and the variation of cloud droplet concentration. *Geofisica pura e applicata*, *43*(1), 243–249. doi: 10.1007/BF01993560

Van Rossum, G., & Drake, F. L. (2009). *Python 3 Reference Manual*. Scotts Valley, CA: CreateSpace.

Wang, Y., & Chen, Y. (2019). Significant climate impact of highly hygroscopic atmospheric aerosols in Delhi, India. *Geophysical Research Letters*, *46*(10), 5535–5545. doi: 10.1029/2019GL082339

Wang, Y., Yu, M., Wang, Y., Tang, G., Song, T., Zhou, P., Liu, Z., Hu, B., Ji, D., Wang, L., Zhu, X., Yan, C., Ehn, M., Gao, W., Pan, Y., Xin, J., Sun, Y., Kerminen, V.-M., Kulmala, M., & Petäjä, T. (2020). Rapid

formation of intense haze episodes via aerosol–boundary layer feedback in Beijing. *Atmospheric Chemistry and Physics*, *20*(1), 45–53. doi: 10.5194/acp-20-45-2020

Wiedensohler, A. (1988). An approximation of the bipolar charge distribution for particles in the submicron size range. *Journal of Aerosol Science*, *19*(3), 387–389. doi: 10.1016/0021-8502(88)90278-9

Yu, J., Wang, Y., & Liu, M. (2020). Mechanisms of an extreme fog and haze event in the megacities of central and eastern China. *Meteorology and Atmospheric Physics*, 1–17. doi: 10.1007/s00703-020-00737-2

Zheng, G. J., Duan, F. K., Su, H., Ma, Y. L., Cheng, Y., Zheng, B., Zhang, Q., Huang, T., Kimoto, T., Chang, D., Pöschl, U., Cheng, Y. F., & He, K. B. (2015). Exploring the severe winter haze in Beijing: the impact of synoptic weather, regional transport and heterogeneous reactions. *Atmospheric Chemistry and Physics*, *15*(6), 2969–2983. doi: 10.5194/acp-15-2969-2015